Article

Analytical Attitude Guidance Planner for Multiple Ground Targets Acquisitions

Andrea Carbone *, **Dario Spiller** and **Fabio Curti**

School of Aerospace Engineering, Sapienza University of Rome, Via Salaria 851, 00138 Rome, Italy
* Correspondence: and.carbone@uniroma1.it

Abstract: This paper focuses on the development of a guidance methodology for the planning of multiple ground target acquisition. Specifically, the work addresses the problem of the lack of an attitude guidance planner (AGP) aboard a remote sensing satellite. In general, the guidance is computed offline and uploaded by ground control to the space segment, i.e., satellites are not responsible for the guidance generation but they only perform control algorithms to track the guidance profiles provided by the ground segment. Overall, this limits the mission flexibility and efficiency, affecting the capability of autonomous satellite decisions. This choice is driven by the fact that the numerical algorithms used to optimize the attitude guidance trajectory require high computational effort to be implemented directly on the satellite computer. Therefore, the aim of this work is to design an analytical AGP solution to solve this problem by requiring low computational effort, making it suitable for real-time applications on on-board flight hardware. In this way, the satellite's guidance, navigation, and control (GNC) module would become completely autonomous and independent of ground control, which will only have to indicate the targets to be acquired so that the satellite can generate its own guidance for the GNC module. The AGP analytical solution for multiple ground target acquisition is evaluated by means of phases: the first phase is named the $APPG$ (attitude point-to-point generator) and it aims to generate the point-to-point guidance to start the ground target acquisition. The second phase is named the $ATPG$ (attitude target pointing generator) and it generates the reference guidance to maintain the payload view axis pointing toward the ground target. The two phases joined together give the whole guidance needed to observe ground target points by means of an analytical closed-form solution.

Keywords: attitude guidance planner; multiple ground targets; on-board guidance generator; analytical solution

1. Introduction

Since the first steps, space science has shown interest in Earth remote sensing systems, particularly those deployed on satellites, which provide a repetitive and coherent view of the earth that is invaluable for monitoring short-term and long-term changes and the impact of human activities [1,2]. In recent years, thanks to technological advancements, Earth observation has become fundamental for everyday life, for instance, it is possible to identify wildfires, eruptions, and more generally natural hazards and disasters [3,4], also thanks to technological improvements such as distributed systems [5], which are not yet fully exploited in satellite remote sensing. For the branch of science dealing with disaster monitoring, it is of the utmost importance that the location identification of the disaster occurs in a short time, or better that it occurs in real time. However, with the technology on-board current remote sensing missions, such real-time detection of extreme events is not possible. Indeed, the image acquisitions are programmed offline by the ground control and it is not possible to change them on-board. This is due to the fact that guidance must be evaluated in order to minimize some parameters, such as maneuver time or consumption,

and it can be performed by means of numerical optimization algorithms which usually require high computational effort.

Efforts in designing innovative techniques for planning attitude maneuvers in computationally efficient ways are reported in the recent literature. For instance, Kornfeld [6] propose a genetic algorithm to optimize an attitude guidance planner (AGP) by imposing boundary constraints. Furthermore, Wu et al. [7] used a metaheuristic method to obtain a time-optimal attitude maneuver by imposing boundary and pointing constraints. Again, in another work, Wu and Han [8] studied an energy-optimal AGP under complex constraints by exploiting the solution of a quadratic programming problem. Melton proposed a solution for time-optimal, constrained satellite reorientation maneuvers by using particle swarm optimization (PSO) [9]. In [10] and [11], Spiller et al. proposed a method to solve the problem of time-optimal satellite reorientation maneuvers with boundary and path constraints by using the PSO and the inverse dynamics approach.

The problem of autonomous on-board AGPs has been already addressed in the recent remote sensing literature, where the ability of taking autonomous decisions has been generally recognized as playing a fundamental role in future missions. For example, the detection of natural disasters (such as forest fires, floods, eruptions, etc.) must occur in real time to avoid large-scale losses and seriously endanger human life. This means that the satellite must be able not only to select by itself the areas of interest to be acquired but also to generate the guidance needed to perform the task. An overview of the problem is well given in [12], where a discussion of current issues and possible solutions is presented. Many researchers are focusing on this problem: in [13], S. De Florio et al. deal with the problem of planning and scheduling operations for a remote sensing satellite constellation; the same problem is addressed in [14], where G. Stock et al. developed a ground software to automate the optimization of satellite constellation operations and validated the software in an operational mission; Y. Song et al. designed an autonomous ground planner to acquire ground targets according to emergency levels [15]. An even more cutting-edge solution is proposed in [16], where S. Liu and J. Yang designed a satellite task planner by means of a heuristic search algorithm based on a symmetric recurrent neural network. Many other works can be listed as interesting solutions to the problem, such as [17–25]. All these works report elegant solutions to perform an AGP, but they need a ground segment to implemented them since they require high computational capabilities. Therefore, in general, AGP cannot be evaluated on-board the satellite, but have to be computed offline and uploaded by ground control. This solution could limit the mission flexibility and efficiency, impacting the capability to plan the acquisition of new targets and reducing the number of targets that may be acquired.

Based on the recent advent of small satellites [26] and the exploitation of machine learning for remote sensing tasks [27–30], some authors have already explored the opportunities provided by on-board processing of remote sensing images [31–35]. However, all these applications would quite benefit from on-board autonomous planning capabilities, so that the satellites can entirely focus on observing and monitoring hazards and disasters on the planet.

The aim of this work is to design an AGP in order to obtain an algorithm that requires a very limited computational effort to make it applicable in real-time on-board applications. Specifically, the work focuses on the design of an autonomous satellite maneuver planner for multiple ground target acquisition, having as input the ground targets positions with respect to the Earth-centered Earth-fixed ($ECEF$) reference frame (expressed in terms of latitude (μ), longitude (λ), and altitude/elevation (h) above mean sea level) and the time in which each acquisition should be performed (t_{start}). The AGP outputs are represented by reference profiles that must be tracked by any external controller (linear PID controller, LQR controller, SDRE controller, etc.). Indeed, guidance and control can be split so that the former provides the reference kinematics, i.e., the quaternion and angular velocity profiles, while the latter tries to track them as well as possible. Thus, the goal of the paper is to develop a reference guidance policy for the GNC module in terms of attitude kinematics

profiles (quaternions, angular velocities, and angular accelerations) and control policies. An analytical optimal closed-form solution was developed to perform an AGP and has been carried out by dividing the problem into two parts: in the first phase, the satellite attitude must be brought from the current state (at initial time t_0) to the desired final state in order to start ground target acquisition (t_{start}). Therefore, the first phase can be seen as a boundary value problem that can be solved by a point-to-point maneuver in a fixed time ($\Delta T_{APPG} = t_{start} - t_0$) and is named $APPG$ (attitude point-to-point generator). In this phase, the guidance is approximated by means of polynomials, which always return a mathematical solution, but not all of them are exploitable. In fact, physical constraints for the maximum allowed control torque and angular velocity are considered in this work. The second phase aims to keep the payload line of sight pointed toward the ground targets for the time required for acquisition (t_{ac}). This phase is named the attitude target pointing generator ($ATPG$). The solution of this phase is achieved by geometric resolution, finding the attitude at each instant through two Euler rotations (around a principal axis). Although from a chronological point of view the two steps take place as indicated above, the algorithm requires them to be performed in reverse, i.e., the $ATPG$ is evaluated before the $APPG$. This is because the $APPG$ must take into account the final desired state at time t_{start} before executing the point-to-point maneuver. For this reason, the $ATPG$ is presented first, followed by the $APPG$.

The paper is organized as follows. In Section 2, the orbital and attitude dynamics of the satellite are reported along with the solution setup. Section 3 describes the attitude target pointing generator phase, i.e., the solution strategy to track the ground targets, while Section 4 deals with the attitude point-to-point generator, i.e., the first part of the proposed solution. In Section 5, numerical simulations and results are carried out. Finally, concluding remarks are provided in Section 6.

2. Problem Description and Proposed Solution

In this section, we will provide all the necessary elements to understand the problem and the proposed solution. Hence, a description of the reference frames is given in Section 2.1, the dynamical model ruling the satellite motion is reported in Section 2.2, and the description of the physical constraints to be respected during the maneuver and the proposed kinematic approach are described in Section 2.3. Finally, Section 2.4 shows the outline of the proposed solution.

2.1. Reference Frames Review

Before writing the dynamical model employed for the analysis, the required reference frames are reviewed in order to provide the right background for the description of the problem [36].

Earth-Centered Inertial (ECI) The ECI coordinate system has its origin in the Earth's center of mass and it is fixed with respect to the stars. The Z_{ECI} axis is aligned with the Earth's rotational axis and points to the north, the X_{ECI} axis points in the direction of the *vernal equinox*, and the Y_{ECI} axis completes the right-handed orthogonal reference system.

Earth-Centered Earth-Fixed (ECEF) This reference frame has the same origin and the same Z axis ($Z_{ECEF} = Z_{ECI}$) as the ECI frame but rotates with the Earth. The X_{ECEF} is in the equatorial plane and points to the Greenwich meridian, while the Y_{ECEF} is taken in order to have a right-handed orthogonal reference system.

Local-Vertical Local-Horizontal (LVLH) It has the origin in the satellite's center of mass, Z_{LVLH} points to the center of the Earth, and X_{LVLH} is parallel to the local horizontal plane (which is the plane normal to the radial position vector connecting the center of the Earth and the satellite), its orientation is such that the satellite's velocity vector is contained in the ($X_{LVLH} - Z_{LVLH}$) plane, and its positive direction is taken to be

concordant with the satellite velocity vector direction. The Y_{LVLH} axis is taken to form a right-handed orthogonal reference system.

Body-Fixed (BF) This frame corresponds to the satellite's principal inertia axes reference frame centered on its center of mass. The *BF* frame is useful to describe the attitude of the satellite. Indeed, the nominal reference attitude of the satellite is often given when the BF frame is aligned with the LVLH frame, and the attitude is described as the displacement of the BF frame with respect to the *LVLH* frame.

Payload Reference Frame (PRF) In this work, the payload consists of a camera mounted with a displacement with respect to the *BF* origin, as shown in Figure 1. Point O_3 identifies the center of the charge-coupled device (*CCD*), which is the camera detector. The *PRF* frame has Z_{PRF} axis aligned with the optical axis and the other two axes (X_{PRF}, Y_{PRF}) are taken to be a right triad. This reference frame is fixed with respect to the BF reference frame, so its rotational matrix R_{BF}^{PRF} is constant and is the payload mounting matrix.
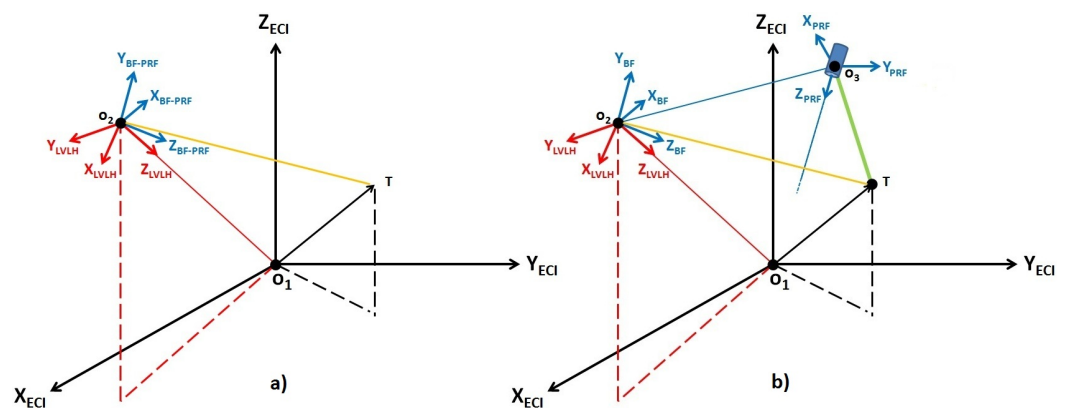

Figure 1. Geometric scheme of reference frames without roto-translation between *BF* and *PRF* (**a**) and with roto-translation between *BF* and *PRF* (**b**).

The reference frames described above are related to our problem as depicted in Figure 1. The geometry behind this problem is not intuitive, since the payload mounting matrix is formed by a roto-translation with respect to the *BF*, and generally the camera view axis (Z_{PRF}) is not centered in the *BF* origin. This point is represented in Figure 1a,b, in which the ground target is indicated with the letter *T* and each reference frame is represented with different colors: the *ECI* is black, the *LVLH* is red, and the *BF-PRF* is blue. The latter are chosen with the same color since they move jointly. In Figure 1a, the origins of *PRF* and *BF* coincide, and any rotation of the satellite does not change the magnitude of the vector $\overrightarrow{O_2T}$ providing the position of the target *T* in *PRF* (but the $\overrightarrow{O_2T}$ components in *PRF* and *BF* change). In the case shown in Figure 1b, instead, *PRF* is displaced and rotated with respect to *BF* and, when a rotation of the satellite is performed, the vector $\overrightarrow{O_3T}$ changes both magnitude and direction in *PRF*, thus modifying the pointing geometry. This configuration makes the problem strongly non-linear and is the one considered in this work. It is worth noting that, at the state of the art, while payload rotation must necessarily be considered, displacement may not be. In fact, the pointing error resulting from displacement is well beyond the actual capabilities of the sensors and actuators. However, in this paper, the general configuration in Figure 1b is considered to make the *AGP* algorithm robust for possible future applications where navigation (attitude sensors) and/or control (actuators) may require much more refined pointing accuracy.

2.2. Dynamical Model

The orbital dynamic is integrated into the *ECI* reference frame and can be written as

$$
\begin{cases}
\dot{\mathbf{r}} = \mathbf{v} \\
\dot{\mathbf{v}} = \mathbf{g} + \mathbf{a}_p
\end{cases}
\tag{1}
$$

where $\mathbf{r} = [x, y, z]$ and $\mathbf{v} = [v_x, v_y, v_z]$ are respectively the position and velocity vector of the satellite, $\mathbf{g}$ is the Earth gravitational acceleration vector, and $\mathbf{a}_p$ represents the acceleration due to orbit perturbations (drag, solar radiation pressure, third body, etc). The satellite attitude is described by using quaternions, with the attitude matrix expressed as a homogeneous quadratic function of their elements. The quaternion $\mathbf{q}$ is written as $\mathbf{q} = [q_0; \mathbf{q}_{1:3}]$ [37,38], where q_0 is the scalar component, $\mathbf{q}_{1:3} \in \mathbf{R}^3$ is the vector component, and $||\mathbf{q}|| = \sqrt{q_0^2 + q_1^2 + q_2^2 + q_3^2} = 1$. For a rigid satellite, the non-linear dynamic equations are expressed as reported in [39],

$$
\begin{cases}
\dot{\mathbf{q}} = \frac{1}{2}\mathbf{\Omega}(t)\mathbf{q}(t) \\
\mathbf{I}\dot{\omega} + \omega \times \mathbf{I}\omega = \mathbf{u}_c + \mathbf{u}_p
\end{cases}
\tag{2}
$$

where ω is the satellite angular velocity expressed in the *BF* reference frame, $\mathbf{I}$ is the inertia tensor, $\mathbf{u}_c$ is the control torque, and $\mathbf{u}_p$ is the perturbation torque, where usually $||\mathbf{u}_c|| > ||\mathbf{u}_p||$. The matrix Ω is

$$
\mathbf{\Omega} = \begin{pmatrix} 0 & -\omega^T \\ \omega & -[\omega\times] \end{pmatrix}
\tag{3}
$$

where $[\omega\times]$ is the anti-symmetric matrix of the angular velocity. It is worth pointing out that, as aforementioned, the aim of this work is not to find a control providing the planned motion, but the motion required to perform a specific task. Thus, the attitude dynamics model in Equation (2) is not used to evaluate the control law, but only to derive the restrictions on the angular accelerations from the constraints on the control values (as shown in the next section).

2.3. Physical Constraints

Before describing the outline of the problem resolution, the physical constraints to be respected are described. A correct maneuver is generated if it is feasible with respect to the imposed path constraints, such as those related to control torque and angular velocity.

2.3.1. Angular Velocity Constraint

High values of the angular velocity would cause unexpected system behaviors, such as large deformations of flexible appendages (so that the satellite could no longer be treated as a rigid body). Furthermore, star trackers could not be able to work if the angular velocity exceeds their operative threshold. Thus, a restriction on angular velocity is imposed and it is expressed as an inequality constraint given by

$$
|\omega_i(t)| \leq \omega_{max}, \quad i = x, y, z,
\tag{4}
$$

where ω_{max} is the maximum allowed angular velocity.

2.3.2. Mapping the Control Constraint to a Kinematic Constraint

Considering the limited capabilities of control actuators and the presence of perturbations, the restriction on control torque is expressed as an inequality constraint for each component in *BF*

$$
|u_{c_i}(t) + u_{p_i}(t)| \leq u_{max}, \quad i = x, y, z,
\tag{5}
$$

where u_{max} is a parameter designed to assure that the control torque $u_{c_i}(t)$ is consistent with the planned satellite kinematic also considering the perturbations. Since the goal of this work is to find an analytical solution without using attitude dynamics, it is useful to translate the control constraint in Equation (5) in a limitation of the angular acceleration. The $u_{c_i}(t)$ components, with $i = x, y, z$, are written as a function of angular velocity and angular acceleration by using Equation (2):

$$
\begin{aligned}
|I_x \dot{\omega}_x + (I_z - I_y)\omega_y\omega_z| &\leq u_{max} \\
|I_y \dot{\omega}_y + (I_x - I_z)\omega_x\omega_z| &\leq u_{max} \\
|I_z \dot{\omega}_z + (I_y - I_x)\omega_y\omega_x| &\leq u_{max}
\end{aligned}
\tag{6}
$$

By applying the triangle inequality and substituting $\omega_y = \omega_z = \omega_{max}$, Equation (6) can be rewritten as follows

$$
\begin{aligned}
|I_x \dot{\omega}_x + (I_z - I_y)\omega_y\omega_z| &\leq |I_x \dot{\omega}_x| + |(I_z - I_y)\omega_{max}^2| \leq u_{max} \\
|I_y \dot{\omega}_y + (I_x - I_z)\omega_x\omega_z| &\leq |I_y \dot{\omega}_y| + |(I_x - I_z)\omega_{max}^2| \leq u_{max} \\
|I_z \dot{\omega}_z + (I_y - I_x)\omega_y\omega_x| &\leq |I_z \dot{\omega}_z| + |(I_y - I_x)\omega_{max}^2| \leq u_{max}
\end{aligned}
\tag{7}
$$

Imposing the equality condition in the last component of Equation (7), the following equations are obtained

$$
\begin{aligned}
\dot{\omega}_{max_x} &= \frac{u_{max} - |(I_z - I_y)\omega_{max}^2|}{I_x} \\
\dot{\omega}_{max_y} &= \frac{u_{max} - |(I_x - I_z)\omega_{max}^2|}{I_y} \\
\dot{\omega}_{max_z} &= \frac{u_{max} - |(I_y - I_x)\omega_{max}^2|}{I_z},
\end{aligned}
\tag{8}
$$

where $\dot{\omega}_{max_i} \triangleq |\dot{\omega}_i|$ $(i = x, y, z)$ by definition is the value of $\dot{\omega}_i$ such that, for any combination of achievable satellite angular velocities, the control constraint in Equation (5) is satisfied. Hence, given u_{max}, we choose $\dot{\omega}_{max_i}$ as the maximum allowed angular acceleration

$$
|\dot{\omega}_i(t)| \leq \dot{\omega}_{max_i}, \quad i = x, y, z.
\tag{9}
$$

For simplicity, a unique value is chosen by taking $\dot{\omega}_{max} = \min(\dot{\omega}_{max_i})$, i.e.,

$$
|\dot{\omega}_i(t)| \leq \dot{\omega}_{max}, \quad i = x, y, z.
\tag{10}
$$

Equations (4) and (10) are kinematic constraints and will be used in the *APPG* phase to generate a feasible path by means of an analytical approach. A polynomial approximation is exploited for each component of the angular velocity vector. With this technique, both the boundary conditions and the dynamical constraints are directly satisfied and the guidance is obtained in a closed-form analytical solution. It is worth pointing out that the attitude dynamics will no longer be taken into consideration, in fact, the manuscript operates with kinematics only to design a reference guidance policy in terms of quaternion, angular velocities, and angular accelerations.

2.4. Solution Setup

This work aims at developing an APG strategy to acquire images of multiple ground targets. By having as input the required starting acquisition time (t_{start}) and the *ECEF* ground targets positions (expressed in terms of latitude (μ), longitude (λ), and altitude/ elevation (h) above mean sea level), the *AGP* task is to generate the reference guidance. The reference guidance brings at first the satellite to the right initial position and then makes it follow the right pointing path. Therefore, the entire guidance can be split into two phases, and each phase can be solved with a different approach. The two phases are briefly explained below.

First phase: the problem is to modify the attitude from any initial condition to the required initial condition to start image acquisition. This is translated into a boundary value problem that can be solved with a point-to-point solution. From now on we refer to this part as the *attitude point-to-point generator* (*APPG*).

Second phase: the problem focuses on the generation of the reference guidance path ensuring that the camera view axis constantly remains pointed towards the ground target. This phase starts at t_{start} and lasts the time of image acquisition, t_{ac}. We will refer to this phase as the *attitude target pointing generator* (*ATPG*).

The scheme of the proposed solution is shown in Figure 2. Here one can see how the satellite maneuvers from the initial attitude to the target acquisition attitude during the *APPG* phase, while the target tracking is performed during the *ATPG*. Furthermore, it is relevant to note that the solution is evaluated starting from the *ATPG* phase, i.e., the maneuver is planned in the opposite direction with respect to the time evolution. This is why, in the following sections, the *ATPG* is described in Section 3 and the *APPG* is described in Section 4.
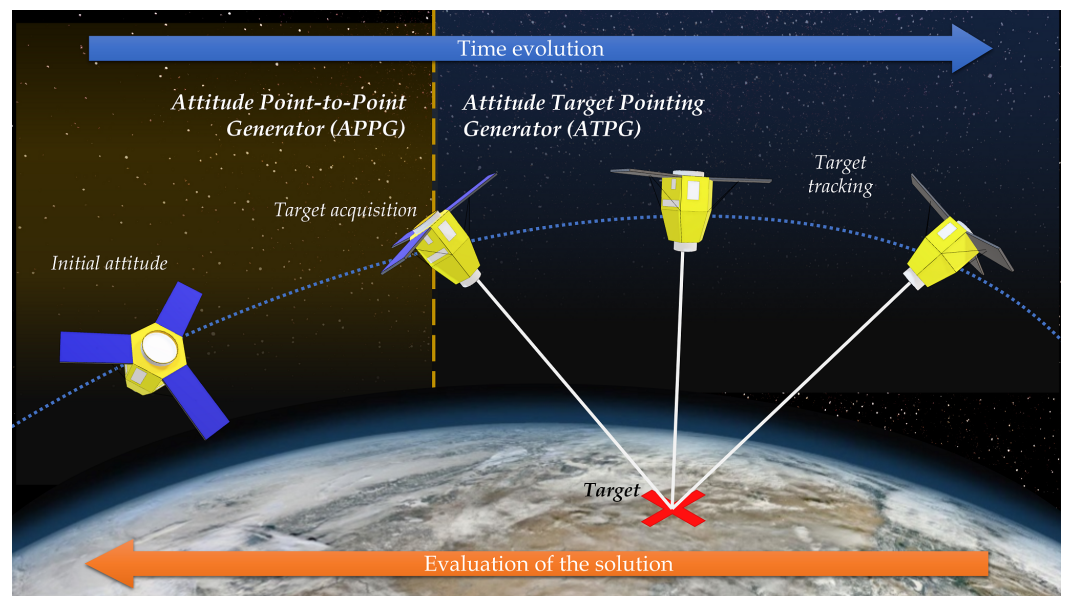

Figure 2. Illustration of the proposed solution. The maneuver is split into two phases, first *APPG* and then *ATPG*, but the solution is evaluated starting from *ATPG*.

3. Attitude Target Pointing Generator

The *ATPG* phase produces the reference attitude profile required to acquire the ground target, i.e., to maintain the camera view axis Z_{PRF} aligned with the position unit vector of the ground target $\overrightarrow{O_3T}$. This phase is performed at a user-defined operative frequency so that, at regular time intervals, it provides the attitude guidance to track the ground target. The analytical *ATPG* solution is carried out by using two consecutive Euler rotations ($\theta_{1,2}$) around two different principal axes ($\hat{\mathbf{e}}_{1,2}$):

1. The first rotation occurs around the unit vector $\widehat{O_2O_3}$ and it has the purpose of bringing the Z_{PRF} axis to lay on the plane identified by $\widehat{O_2O_3} - \widehat{O_2T}$, without modifying either the direction or the magnitude of $\overrightarrow{O_3T}$ (as shown in Figure 3):

$$\begin{cases} \hat{\mathbf{e}}_1 = \widehat{O_2O_3} \\ \theta_1 = \text{atan2}(\sin\theta_1, \cos\theta_1) \end{cases} \tag{11}$$

where $\sin\theta_1 = ||\hat{\mathbf{n}}_1 \times \hat{\mathbf{n}}_2||$, $\cos\theta_1 = \hat{\mathbf{n}}_1 \cdot \hat{\mathbf{n}}_2$ and

$$\hat{\mathbf{n}}_1 = \frac{\widehat{O_2T} \times \widehat{O_2O_3}}{||\widehat{O_2T} \times \widehat{O_2O_3}||}, \quad \hat{\mathbf{n}}_2 = \frac{Z_{PRF} \times \widehat{O_2O_3}}{||Z_{PRF} \times \widehat{O_2O_3}||}. \tag{12}$$
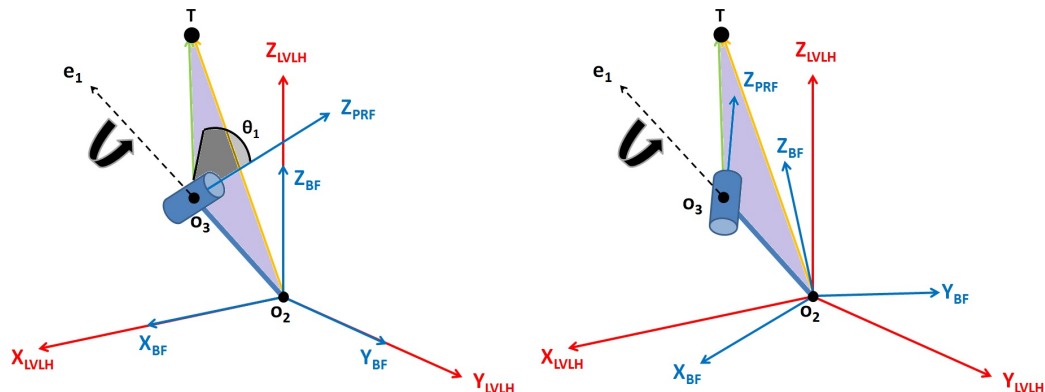

Figure 3. First rotation around $\widehat{O_2O_3}$: the *PRF* is represented before (**left**) and after (**right**) the rotation.

2. The second rotation brings the view axis of the camera Z_{PRF} to coincide with the $\widehat{O_3T}$ direction by means of an Euler's rotation around a principal axis, such that

$$\begin{cases} \hat{\mathbf{e}}_2 = \hat{\mathbf{n}}_1 \\ \theta_2 = \beta_f - \beta_0 \end{cases} \tag{13}$$

where, with respect to Figure 4, $\beta_0 = \cos^{-1}(\widehat{O_2O_3} \cdot \widehat{O_2T})$, $\beta_f = \pi - \alpha - \gamma_f$, $\gamma_f = \sin^{-1}(\sin\alpha||\overrightarrow{O_2O_3}||/||\overrightarrow{O_2T}||)$ and α is equal to the angle between $\widehat{O_2O_3}$ and Z_{PRF}.
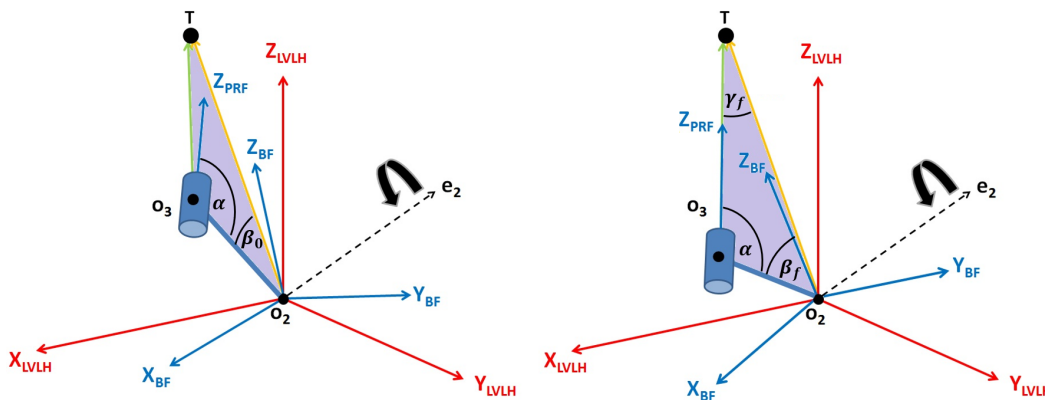

Figure 4. Second rotation around $\hat{\mathbf{n}}_1$: the *PRF* is represented before (**left**) and after (**right**) the rotation.

Therefore, the discrete quaternion time-history can be obtained by repeating, at each time instant, the aforementioned procedure and the equation $\mathbf{q} = [\cos(\theta/2); \hat{\mathbf{e}}\sin(\theta/2)]$. It is noteworthy that, when $O_2 \equiv O_3$, the first step becomes meaningless, whereas it can be easily demonstrated that the second step reduces to a rotation of an angle $\theta_2 = \cos^{-1}(\widehat{O_2T} \cdot Z_{PRF}) = \pi - \alpha - \beta_0$ (as $\gamma_f = 0$) after substituting the direction $\overrightarrow{O_2O_3}$ with any line in the plane given by Z_{PRF} and $\widehat{O_2T}$ and the normal to this plane with $\hat{\mathbf{n}}_1$.

4. Attitude Point-to-Point Generator

Generally, the satellite's initial attitude is far away from the initial attitude required by the *ATPG* phase. For instance, when passing from the old ground target to the new ground target, the satellite must be maneuvered from the old attitude to the new required

pointing direction. This problem can be identified as a boundary value problem in which the constraints of Equations (4) and (10) must be satisfied during the entire path. In the *APPG* phase, the guidance is approximated by means of polynomials which always return mathematical solutions for the point-to-point problem even though their feasibility is not guaranteed and must be verified. The entire maneuver is split into three different steps to obtain an analytical solution, verify the boundary conditions, and reach the desired attitude. The three steps are schematized in Figure 5 and summarized in the following list.
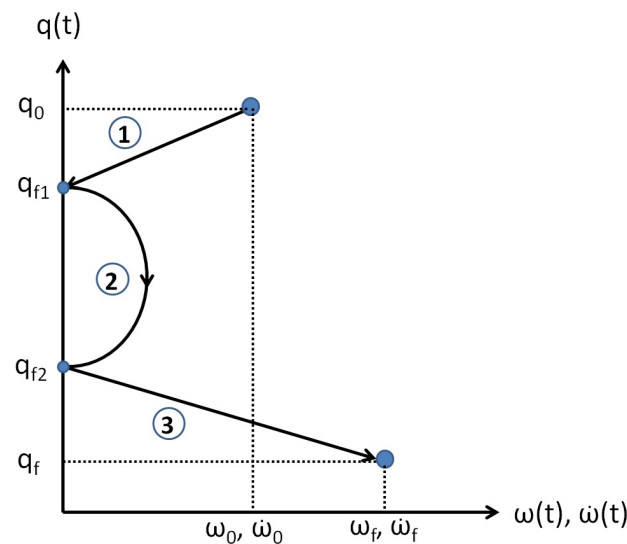

Figure 5. Conceptual scheme of the three *APPG* steps. This scheme is valid for each component of ω and $\dot{\omega}$, the subscript i, $i = x, y, z$ has been removed for simplicity. The trajectories are only for clarification purposes and not descriptive of a real scenario.

Step 1. The satellite arrests its motion and reaches its final attitude $\mathbf{q}_{f_1}$.

Step 2. A rest-to-rest maneuver from $\mathbf{q}_{f_1}$ to a proper switching attitude $\mathbf{q}_{f_2}$ is performed.

Step 3. The satellite motion is accelerated from $\mathbf{q}_{f_2}$ until it reaches the final attitude $\mathbf{q}_f$, the final angular velocity and final acceleration.

The whole path ①-②-③ in Figure 5 changes as a function of $\mathbf{q}_{f_1}$ and $\mathbf{q}_{f_2}$ which depend on the variables t_{f_1}, t_{f_2}, and t_{f_3}, representing the duration of each step, as will be shown in the following paragraphs. The objective of this work is to achieve a guidance trajectory of minimum duration. Consequently, the variables $(t_{f_1}, t_{f_2}, t_{f_3})$ must be selected so that the entire guidance path generates a fast (near minimum-time) maneuver satisfying the constraints of maximum speed and angular acceleration. The evaluation of the guidance is provided by calculating step 1 and step 3, whose results are used as input in step 2.

APPG-Step 1.

Starting from the initial conditions, the attitude guidance is generated to slow the satellite down to a stop. Hence, with reference to Figure 5, boundary constraints are imposed only on angular velocity and acceleration as

$$\begin{cases} \omega_i(0) = \omega_{i_0}; \ \omega_i(t_{f_1}) = 0 \\ \dot{\omega}_i(0) = \dot{\omega}_{i_0}; \ \dot{\omega}_i(t_{f_1}) = 0, \end{cases} \tag{14}$$

where t_{f_1} is the maneuver time of this first phase and $i = x, y, z$. The boundary conditions are four ($m = 4$) and the degree of the polynomial is equal to $n = m - 1 = 3$ (the number of polynomial coefficients is equal to the degree plus one). Thus, the polynomial expression of $\omega_i(t)$ can be expressed as

$$\omega_i(t) = a_{i3}t^3 + a_{i2}t^2 + a_{i1}t + a_{i0}, \tag{15}$$

where $[a_{i3}, a_{i2}, a_{i1}, a_{i0}]$ are the polynomial coefficients. The conditions in Equation (14) can be used to evaluate the four polynomial coefficients of the ith angular velocity component in Equation (15). A system of four equations with four unknowns is obtained

$$\begin{cases} a_{i0} = \omega_{i_0}; & a_{i3}t_{f_1}^3 + a_{i2}t_{f_1}^2 + a_{i1}t_{f_1} + a_{i0} = 0 \\ a_{i1} = \dot{\omega}_{i_0}; & 3a_{i3}t_{f_1}^2 + 2a_{i2}t_{f_1} + a_{i1} = 0. \end{cases} \tag{16}$$

By substituting $a_{i0} = \omega_{i_0}$ and $a_{i1} = \dot{\omega}_{i_0}$ in Equation (16), a_{i2} and a_{i3} can be evaluated. Specifically, the expression $a_{i2} = -(\dot{\omega}_{i_0} + 3a_{i3}t_{f_1}^2)/2t_{f_1}$ (carried out from $3a_{i3}t_{f_1}^2 + 2a_{i2}t_{f_1} + \dot{\omega}_{i_0} = 0$) can be included in $a_{i3}t_{f_1}^3 + a_{i2}t_{f_1}^2 + a_{i1}t_{f_1} + \omega_{i_0} = 0$:

$$a_{i3}t_{f_1}^3 - \frac{\dot{\omega}_{i_0}t_{f_1} + 3a_{i3}t_{f_1}^3}{2} + \dot{\omega}_{i_0}t_{f_1} + \omega_{i_0} = 0 \rightarrow a_{i3} = (2\omega_{i_0} + \dot{\omega}_{i_0}t_{f_1})/t_{f_1}^3. \tag{17}$$

By substituting the expression of a_{i3} in Equation (17) in $a_{i2} = -(\dot{\omega}_{i_0} + 3a_{i3}t_{f_1}^2)/2t_{f_1}$, the expression of a_{i2} as a function of t_{f_1} is found as

$$a_{i2} = -\frac{\dot{\omega}_{i_0}}{2t_{f_1}} - \frac{6\omega_{i_0} + 3\dot{\omega}_{i_0}t_{f_1}}{2t_{f_1}^2} = -\frac{3\omega_{i_0} + 2\dot{\omega}_{i_0}t_{f_1}}{t_{f_1}^2}. \tag{18}$$

Hence, the four polynomial coefficients of the ith angular velocity component are obtained as a function of the final time t_{f_1} and the corresponding boundary conditions:

$$\begin{cases} a_{i0} = \omega_{i_0} \\ a_{i1} = \dot{\omega}_{i_0} \\ a_{i2} = -(3\omega_{i_0} + 2\dot{\omega}_{i_0}t_{f_1})/t_{f_1}^2 \\ a_{i3} = (2\omega_{i_0} + \dot{\omega}_{i_0}t_{f_1})/t_{f_1}^3. \end{cases} \tag{19}$$

The final time t_{f_1} of the polynomial is a free parameter and must be selected in order to calculate the coefficients a_{i2} and a_{i3}, defining a trajectory matching the constrain conditions (Equations (4) and (9)). Even though it is feasible at the boundaries, the guidance must be verified to check that the maximum or the minimum values of $\omega_i(t, t_{f_1})$ and $\dot{\omega}_i(t, t_{f_1})$ are less than or equal to the allowed limits. The time $t_{\omega_{max}}$ at which $\omega_i(t)$ attains its extreme value is evaluated by imposing $\dot{\omega}_i(t)$ equal to zero, thus having

$$t_{\omega_{max}}^{I,II} = \frac{-a_{i2} \pm \sqrt{a_{i2}^2 - 3a_{i3}a_{i1}}}{3a_{i3}}. \tag{20}$$

Using Equation (19) in Equation (20), the two solutions are

$$t_{\omega_{max}}^{I,II} = \frac{((3\omega_{i_0} + 2\dot{\omega}_{i_0}t_{f_1}) \pm (3\omega_{i_0} + \dot{\omega}_{i_0}t_{f_1}))t_{f_1}}{6\omega_{i_0} + 3\dot{\omega}_{i_0}t_{f_1}} \rightarrow \begin{cases} t_{\omega_{max}}^{I} = t_{f_1} \\ t_{\omega_{max}}^{II} = \frac{\dot{\omega}_{i_0}t_{f_1}^2}{6\omega_{i_0} + 3\dot{\omega}_{i_0}t_{f_1}} \end{cases} \tag{21}$$

The $t_{\omega_{max}}^{I}$ solution is the imposed boundary condition, while $t_{\omega_{max}}^{II}$ provides the required information. Referring to $t_{\omega_{max}}^{II}$ as $t_{\omega_{max_1}}$, where the subscript 1 stands for the *first step*, the condition $|\omega_i(t = t_{\omega_{max_1}})| \leq \omega_{max}$, which is an expression depending the free parameter t_{f_1}, must be verified.

The same approach can be exploited to find the condition for which $\dot{\omega}_i(t)$ reaches its maximum value. Indeed, by imposing $\ddot{\omega}_i(t) = 0$ one can obtain

$$t_{\dot{\omega}_{max}} = -\frac{a_{i2}}{3a_{i3}} = \frac{(3\omega_{i_0} + 2\dot{\omega}_{i_0}t_{f_1})}{(2\omega_{i_0} + \dot{\omega}_{i_0}t_{f_1})}\frac{t_{f_1}}{3}. \tag{22}$$

The condition $|\dot{\omega}_i(t = t_{\dot{\omega}_{max}})| \leq \dot{\omega}_{max}$ depending on the parameter t_{f_1} must be verified. Finally, referring to $t_{\dot{\omega}_{max}}$ as $t_{\dot{\omega}_{max_1}}$, the value of t_{f_1} is chosen to satisfy the constraints

$$\begin{cases} |\omega_i(t = t_{\omega_{max_1}})| \leq \omega_{max}, \\ |\dot{\omega}_i(t = t_{\dot{\omega}_{max_1}})| \leq \dot{\omega}_{max}, \quad i = x, y, z, . \end{cases} \tag{23}$$

In particular, from Equation (23), t_{f_1} is evaluated in order to maximize one condition without exceeding the other one. The analytical procedure will be described in detail in the next section.

The attitude guidance is represented by the quaternion time-history, calculated by using the differential equation of quaternion kinematics, $\dot{\mathbf{q}} = 1/2\,\Omega(t)\mathbf{q}_0$, where $\mathbf{q}_0$ is the initial attitude of the satellite. The solution is retrieved by integrating over the time interval $[0; t_{f_1}]$. Therefore, if the satellite follows the attitude guidance of step 1, represented by the quaternion time history, the rotation would be stopped and the attitude reaches the final condition $\mathbf{q}_{f_1}$.

APPG-Step 2.

From Figure 5, the second step should connect the two quaternions $\mathbf{q}_{f_1}$ and $\mathbf{q}_{f_2}$, which are related to two different states, i.e.,

$$\begin{cases} \mathbf{q}(t_{f_1}) = \mathbf{q}_{f_1} \\ \boldsymbol{\omega}(t_{f_1}) = \boldsymbol{\omega}_{f_1} = 0 \\ \dot{\boldsymbol{\omega}}(t_{f_1}) = \dot{\boldsymbol{\omega}}_{f_1} = 0 \end{cases} \quad \begin{cases} \mathbf{q}(t_{f_2}) = \mathbf{q}_{f_2} \\ \boldsymbol{\omega}(t_{f_2}) = \boldsymbol{\omega}_{f_2} = 0 \\ \dot{\boldsymbol{\omega}}(t_{f_2}) = \dot{\boldsymbol{\omega}}_{f_2} = 0 \end{cases} \tag{24}$$

Since both angular velocity and acceleration are zero, a rest-to-rest guidance law is implemented. The quaternion describing the rotation from $\mathbf{q}_{f_1}$ to $\mathbf{q}_{f_2}$ is

$$\mathbf{q} = \mathbf{q}_{f_1}^c \otimes \mathbf{q}_{f_2} \tag{25}$$

where the superscript c stands for conjugate. Since $\mathbf{q}_{f_1}$ and $\mathbf{q}_{f_2}$ do not change over time, $\mathbf{q}$ is constant and a rest-to-rest guidance law can be implemented. Thus, Euler's rotation can be exploited, i.e., a single rotation (θ_f) around a principal axis ($\hat{\mathbf{e}}$). From the quaternion definition, the axis-angle rotation can be calculated as follows:

$$\begin{cases} \theta_f = \cos^{-1}(q_0) \\ \hat{\mathbf{e}} = \mathbf{q}_{1:3}/\sin(\theta_f/2) \end{cases} \tag{26}$$

Euler's axis-angle rotation allows us to get ω and $\dot{\omega}$ (the magnitudes of $\boldsymbol{\omega}$ and $\dot{\boldsymbol{\omega}}$, not to be confused with the vector components ω_i and $\dot{\omega}_i$) by differentiating θ with respect to time (which is not the case for Euler's angles or quaternions), i.e.,

$$\boldsymbol{\omega} = \dot{\theta}(t)\hat{\mathbf{e}} = \omega\,\hat{\mathbf{e}}, \quad \dot{\boldsymbol{\omega}} = \ddot{\theta}(t)\hat{\mathbf{e}} = \dot{\omega}\,\hat{\mathbf{e}}. \tag{27}$$

The analytical solution is retrieved by approximating the angle θ with a polynomial. The set of boundary conditions that defines a smooth rest-to-rest guidance law contains initial and final rotation angles, angular velocities, and angular accelerations, i.e.,

$$\begin{cases} \theta(0) = 0; \ \theta(t_{f_3}) = \theta_f \\ \omega(0) = 0; \ \omega(t_{f_3}) = 0 \\ \dot{\omega}(0) = 0; \ \dot{\omega}(t_{f_3}) = 0. \end{cases} \tag{28}$$

The boundary conditions of the point-to-point guidance law determine the degree of the polynomial ($m = 6$), thus, a polynomial of degree $n = m - 1 = 5$ is chosen. Hence, $\theta(t)$ is

$$\theta(t) = b_5 t^5 + b_4 t^4 + b_3 t^3 + b_2 t^2 + b_1 t + b_0 \tag{29}$$

$\omega(t)$ and $\dot{\omega}(t)$ are evaluated by time differentiating according to Equation (27). The six b_j coefficients can be evaluated as a function of the final time t_{f_2} by using the conditions in Equation (28), i.e., a system of six equations with six unknowns is obtained

$$\begin{cases} b_0 = 0; & b_5 t^5_{f_2} + b_4 t^4_{f_2} + b_3 t^3_{f_2} + b_2 t^2_{f_2} + b_1 t_{f_2} + b_0 = \theta_f \\ b_1 = 0; & 5 b_5 t^4_{f_2} + 4 b_4 t^3_{f_2} + 3 b_3 t^2_{f_2} + 2 b_2 t_{f_2} + b_1 = 0 \\ b_2 = 0; & 20 b_5 t^3_{f_2} + 12 b_4 t^2_{f_2} + 6 b_3 t_{f_2} + 2 b_2 = 0 \end{cases} \tag{30}$$

By substituting $b_0 = b_1 = b_2 = 0$ and simplifying the other three expressions in Equation (30), the following system is obtained:

$$\begin{cases} b_5 t^5_{f_2} + b_4 t^4_{f_2} + b_3 t^3_{f_2} = \theta_f \\ 5 b_5 t^2_{f_2} + 4 b_4 t_{f_2} + 3 b_3 = 0 \rightarrow b_3 = -(5 b_5 t^2_{f_2} + 4 b_4 t_{f_2})/3 \\ 10 b_5 t^2_{f_2} + 6 b_4 t_{f_2} + 3 b_3 = 0 \rightarrow b_3 = -(10 b_5 t^2_{f_2} + 6 b_4 t_{f_2})/3 \rightarrow b_4 = -\frac{5}{2} b_5 t_{f_2}. \end{cases} \tag{31}$$

By including $b_4 = -\frac{5}{2} b_5 t_{f_2}$ in $b_3 = -(5 b_5 t^2_{f_2} + 4 b_4 t_{f_2})/3$, $b_3 = \frac{5}{3} b_5 t^2_{f_2}$ is evaluated. Then, putting b_3 and b_4 in the first equation of Equation (31), $b_5 = 6 \theta_f / t^5_{f_2}$ is evaluated and the expressions of b_3 and b_4 as a function of t_{f_2} are obtained as $b_3 = 10 \theta_f / t^3_{f_2}$ and $b_4 = -15 \theta_f / t^4_{f_2}$. Thus, the six b_j coefficients can be summed up as a function of the final time t_{f_2} and boundary conditions as

$$\begin{cases} b_0 = b_1 = b_2 = 0 \\ b_3 = 10\, \theta_f / t^3_{f_2} \\ b_4 = -15\, \theta_f / t^4_{f_2} \\ b_5 = 6\, \theta_f / t^5_{f_2}. \end{cases} \tag{32}$$

The final time t_{f_2} is a free parameter and must be selected in order to calculate the coefficients b_3, b_4 and b_5 defining a trajectory matching the constraint conditions. Since the direction of the rotation is fixed, the ith component of the angular velocity and acceleration is no longer free to vary independently from the other components. As a consequence, constraint conditions can be imposed only on the magnitude of $\omega(t)$ and $\dot{\omega}(t)$. If the problem had been in a $2D$ space, as shown in Figure 6a, the maximum magnitude of the angular velocity would have been a function of the angle δ. Since the unit vector $\hat{\mathbf{e}}$ intersects the square side normal to the x axis, $\omega_x = \omega_{max}$, $\omega_y = \omega_x \tan \delta$, and $\|\omega\|_{max} = \sqrt{\omega_x^2 + \omega_y^2} = \omega_x \sqrt{1 + \tan^2 \delta} = \omega_{max} \sqrt{1 + \tan^2 \delta}$.

Performing the analysis along all directions and considering a cube in the 3D space, as in Figure 6b, the same logic can be applied. The components ω_x, ω_y, and ω_z are linked together by

$$\begin{cases} \tan \delta = \dfrac{\omega_y}{\omega_x}, \\ \tan \eta = \dfrac{\omega_z}{\sqrt{\omega_x^2 + \omega_y^2}}. \end{cases} \tag{33}$$
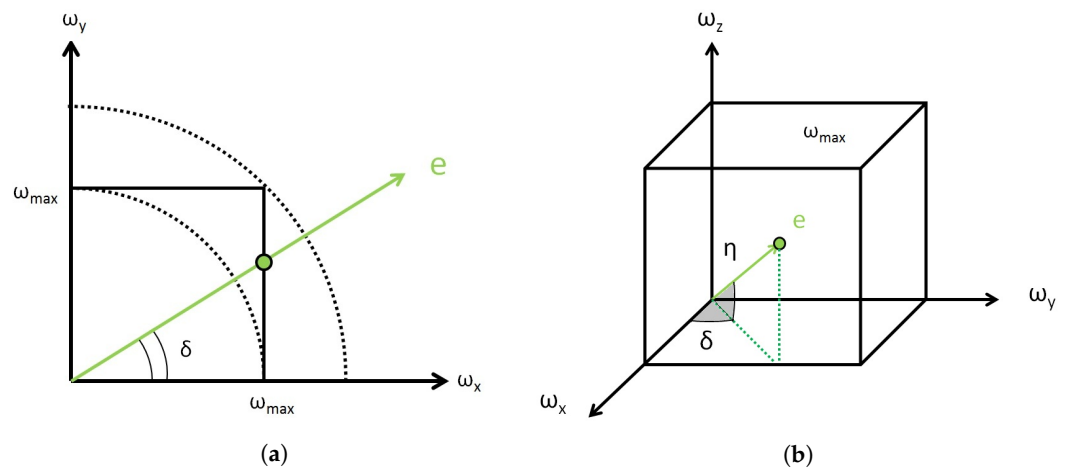
Figure 6. Maximum ω magnitude in the 2D problem (**a**) and in the 3D problem (**b**).

The ith component of the angular velocity normal to the plane intersected by the unit vector **e** is imposed to reach the maximum value. For instance, in Figure 6b, $\omega_x = \omega_{max}$ since the rotation axis (represented with the color green), intersects the surface where the x axis is the normal vector. Then Equation (33) becomes a system with two unknowns and is therefore solvable. The physical constraints for the rest-to-rest guidance law are $|\omega(t)| \leq \omega_{max}$ and $|\dot{\omega}(t)| \leq \dot{\omega}_{max}$. This problem is similar to that treated in the previous step, but with the polynomials $\omega(t)$ and $\dot{\omega}(t)$ one degree higher. As aforementioned, the final time t_{f_2} of the polynomial is the free parameter and must be selected to calculate the coefficients b_3, b_4 and b_5, defining a trajectory matching the imposed constrain conditions. The condition for which $\omega(t)$ assumes its maximum can be evaluated by imposing $\dot{\omega}(t) = 0$,

$$\dot{\omega}(t) = 20b_5 t^3 + 12b_4 t^2 + 6b_3 t = 0 \tag{34}$$

One root of Equation (34) is fixed in the initial instant $t_{\omega_{max}}^I = 0$, which is the boundary condition imposed in Equation (28). The other two solutions, which are the time instants $t_{\omega_{max}}^{II,III}$ at which $\omega(t)$ assume a maximum value, are found by solving a quadratic equation

$$t_{\omega_{max}}^{II,III} = \frac{-3b_4 \pm \sqrt{9b_4^2 - 30b_5 b_3}}{10b_5}. \tag{35}$$

Using Equation (32) in Equation (35), the two solutions are obtained as

$$t_{\omega_{max}}^{II,III} = \frac{3 \pm 1}{4} t_{f_2} \quad \rightarrow \quad \begin{cases} t_{\omega_{max}}^{II} = t_{f_2} \\ t_{\omega_{max}}^{III} = t_{f_2}/2 \end{cases} \tag{36}$$

The solution $t_{\omega_{max}}^{II}$ is the boundary condition imposed at the end of the guidance law. Accordingly, only the condition $|\omega(t = t_{\omega_{max}}^{III})| \leq \omega_{max}$ must be verified, which is a function of the variable t_{f_2}. Let $t_{\omega_{max}}^{III}$ be defined as $t_{\omega_{max_2}}$, where the subscript 2 stands for the *second step*.

The same approach can be exploited to find the condition in which $\dot{\omega}(t)$ reaches its maximum value by imposing

$$\ddot{\omega}(t) = 10b_5 t^2 + 4b_4 t + b_3 = 0 \tag{37}$$

which can be solved as

$$t_{\dot{\omega}_{max}}^{I,II} = \frac{-2b_4 \pm \sqrt{4b_4^2 - 10b_5 b_3}}{10b_5} \underset{\text{Equation (32)}}{=} t_{\dot{\omega}_{max}}^{I,II} = t_{f_2} \frac{3 \pm \sqrt{3}}{6}. \tag{38}$$

This solution is symmetrical with respect to $t_{f_2}/2$ and identifies the two peaks of $\dot{\omega}(t)$. As can be seen from Figure 7, the two solutions have the same magnitude. Thus it can be stated that $|\dot{\omega}(t = t^I_{\dot{\omega}_{max}})| = |\dot{\omega}(t = t^{II}_{\dot{\omega}_{max}})|$. Indeed, given the form of Equation (34), the point of symmetry lies on the t axis so that minimum and maximum have the same absolute value. Therefore, the two solutions in Equation (38), can be summarized as a unique condition. For instance, let $t = t^I_{\dot{\omega}_{max}}$ be defined as $t_{\dot{\omega}_{max_2}}$, where the subscript 2 stands again for the second step. As a consequence, the physical constraints are functions of t_{f_2}.
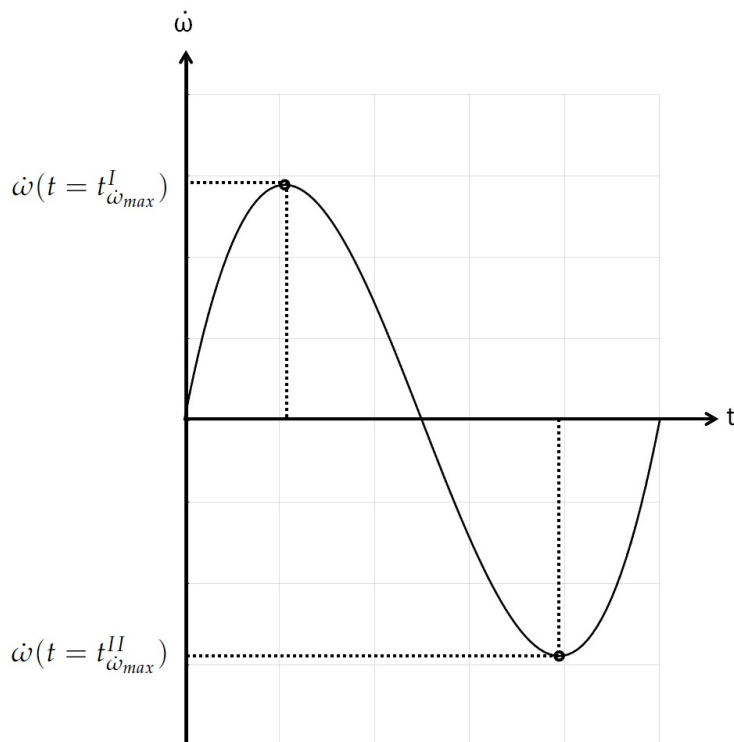

Figure 7. Representation of the symmetrical positions where $|\dot{\omega}|$ gets extreme values.

$$\begin{cases} |\omega(t = t_{\omega_{max_2}})| \le \omega_{max} \\ |\dot{\omega}(t = t_{\dot{\omega}_{max_2}})| \le \dot{\omega}_{max} \end{cases} \tag{39}$$

APPG-Step 3.

Following the scheme in Figure 5, and similarly to step 1, the angular velocity and acceleration leading the satellite to the final conditions are found starting from a steady state and accelerating until the desired angular velocity and acceleration. Boundary constraints are imposed only on angular velocity and acceleration

$$\begin{cases} \omega_i(0) = 0; \ \omega_i(t_{f_3}) = \omega_{i_f}, \\ \dot{\omega}_i(0) = 0; \ \dot{\omega}_i(t_{f_3}) = \dot{\omega}_{i_f}, \quad i = x, y, z, \end{cases} \tag{40}$$

where t_{f_3} is the guidance law time of the third step, and ω_{i_f} and $\dot{\omega}_{i_f}$ are the final condition of each ith component of the angular velocity and acceleration, respectively. The free parameter is t_{f_3}, similar to t_{f_1} in the previous step. Therefore, $t_{\omega_{max_3}}$ and $t_{\dot{\omega}_{max_3}}$ are given as a function of the final time t_{f_3} as well as the physical constraints, i.e.,

$$\begin{cases} |\omega_i(t = t_{\omega_{max_3}})| \le \omega_{max} \\ |\dot{\omega}_i(t = t_{\dot{\omega}_{max_3}})| \le \dot{\omega}_{max}, \quad i = x, y, z. \end{cases} \tag{41}$$

As a consequence, the polynomial trajectories that approximate $\omega_i(t)$ and $\dot{\omega}_i(t)$ in this step are fully defined, i.e., the boundary conditions and the physical constraints are satisfied. The quaternion trajectory can be evaluated by integrating backward the differential equation of quaternion kinematics, i.e., the initial attitude of this guidance law ($\mathbf{q}_{f_2}$) can be evaluated starting from the desired one ($\mathbf{q}_d$) by integrating the differential equation from t_{f_3} to 0.

APPG-Summary.

The aforementioned three steps are given as a function of the final time of each phase, therefore, t_{f_1}, t_{f_2}, and t_{f_3} are the free parameters of the problem. They must be selected in order to verify the physical constraints of each step, i.e., Equation (23), Equation (39), and Equation (41), which are listed together in Table 1.

Table 1. APPG summary considering the most relevant definitions and the imposed path constraints.

Step 1	Step 2	Step 3
Constraints on each component	Constraints on the magnitude only	Constraints on each component
ω_i from Equation (15), $t_{\omega_{max_1}}$ from Equation (22).	ω by differentiating Equation (29), $t_{\dot{\omega}_{max_2}}$ from Equation (38).	ω_i as in Equation (15), $t_{\omega_{max_1}}$ as in Equation (22).
$i = x, y, z$		$i = x, y, z$
$\begin{cases} \|\omega_i(t = t_{\omega_{max_1}})\| \leq \omega_{max} \\ \|\dot{\omega}_i(t = t_{\dot{\omega}_{max_1}})\| \leq \dot{\omega}_{max} \end{cases}$	$\begin{cases} \|\omega(t = t_{\omega_{max_2}})\| \leq \omega_{max} \\ \|\dot{\omega}(t = t_{\dot{\omega}_{max_2}})\| \leq \dot{\omega}_{max} \end{cases}$	$\begin{cases} \|\omega_i(t = t_{\omega_{max_3}})\| \leq \omega_{max} \\ \|\dot{\omega}_i(t = t_{\dot{\omega}_{max_3}})\| \leq \dot{\omega}_{max} \end{cases}$

4.1. Near Optimal Time

As already mentioned above, the objective of this work is to optimize the variables t_{f_1}, t_{f_2}, and t_{f_3} in order to perform the three steps of *APPG* as fast as possible. This condition can be approximated if the three steps occur at maximum angular velocity and acceleration. This statement translates into imposing the equality in the summary equations of Table 1 and thus solving Equation (42).

$$
\begin{aligned}
1 &\to \begin{cases} |\omega_i(t = t_{\omega_{max_1}})| = \omega_{max} \\ |\dot{\omega}_i(t = t_{\dot{\omega}_{max_1}})| = \dot{\omega}_{max} \end{cases} \\
2 &\to \begin{cases} |\omega(t = t_{\omega_{max_2}})| = \omega_{max} \\ |\dot{\omega}(t = t_{\dot{\omega}_{max_2}})| = \dot{\omega}_{max} \end{cases} \\
3 &\to \begin{cases} |\omega_i(t = t_{\omega_{max_3}})| = \omega_{max} \\ |\dot{\omega}_i(t = t_{\dot{\omega}_{max_3}})| = \dot{\omega}_{max} \end{cases}
\end{aligned}
\tag{42}
$$

In this way, it is possible to find the duration of each phase with an analytical closed-form solution, satisfying the constraints of maximum angular velocity and acceleration. It is noteworthy that the proposed analytical solution is not based on the verification of any minimization principle (e.g., the Pontryagin minimum principle), hence the strategy represents a near-optimal time solution focused on computational efficiency.

4.1.1. Maneuver Time for Step 1

Starting from the first constraint in Equation (42), ω_i and $\dot{\omega}_i$ can be written in explicit form as a function of the only unknown t_{f_1}. In fact, the coefficients a_{ij}, $t_{\omega_{max_1}}$, and $t_{\dot{\omega}_{max_1}}$ are functions of t_{f_1}, as stated in Equation (19), Equation (21), and Equation (22). Thus, the two polynomials can be written as follows:

$$\left| \frac{\dot\omega_{i_0}^3 t_{f_1}^3 (2\omega_{i_0} + \dot\omega_{i_0} t_{f_1})}{(6\omega_{i_0} + 3\dot\omega_{i_0} t_{f_1})^3} - \frac{\dot\omega_{i_0}^2 t_{f_1}^2 (3\omega_{i_0} + \dot\omega_{i_0} t_{f_1})}{(6\omega_{i_0} + 3\dot\omega_{i_0} t_{f_1})^2} + \omega_{i_0} \right| = \omega_{max}$$

$$\left| \dot\omega_0 - \frac{(3\omega_{i_0} + 2\dot\omega_{i_0} t_{f_1})^2 t_{f_1}}{3(2\omega_{i_0} + \dot\omega_{i_0} t_{f_1})} \right| = \dot\omega_{max} \tag{43}$$

Equation (43) can be rewritten without the absolute value and the system becomes a system of four equations, two for each absolute value,

$$\frac{\dot\omega_{i_0}^3 t_{f_1}^3 (2\omega_{i_0} + \dot\omega_{i_0} t_{f_1})}{(6\omega_{i_0} + 3\dot\omega_{i_0} t_{f_1})^3} - \frac{\dot\omega_{i_0}^2 t_{f_1}^2 (3\omega_{i_0} + \dot\omega_{i_0} t_{f_1})}{(6\omega_{i_0} + 3\dot\omega_{i_0} t_{f_1})^2} + \omega_{i_0} = \pm \omega_{max}$$

$$\dot\omega_0 - \frac{(3\omega_{i_0} + 2\dot\omega_{i_0} t_{f_1})^2}{3(2\omega_{i_0} + \dot\omega_{i_0} t_{f_1}) t_{f_1}} = \pm \dot\omega_{max} \tag{44}$$

Rearranging the terms in Equation (44),

$$4\dot\omega_{i_0}^3 t_{f_1}^3 + 9\dot\omega_{i_0}^2 (4\omega_{i_0} \pm 3\omega_{max}) t_{f_1}^2 + 108\dot\omega_{i_0} \omega_{i_0}^2 (\omega_{i_0} \pm \omega_{max}) t_{f_1} + 108\omega_{i_0}^2 (\omega_{i_0} \pm \omega_{max}) = 0$$

$$\dot\omega_{i_0} (\dot\omega_{i_0} \pm 3\dot\omega_{max}) t_{f_1}^2 + 6\omega_{i_0} (\dot\omega_{i_0} \pm \dot\omega_{max}) t_{f_1} + (9\omega_{i_0}^2) = 0 \tag{45}$$

While the solution of the second-degree equation is straightforward, the cubic one requires much more mathematical effort. In this work, we follow the solution reported by Neumark et al. [40]. As a consequence, Equation (45) is solvable in closed form: for each ith component of the angular velocity, six roots can be calculated from the first equation, which are identified with the symbol $t_{f_1}^{\omega_i}$; three of the six solutions are given by imposing $+\omega_{max}$ and the other three by imposing $-\omega_{max}$. Then, for each ith component of the angular acceleration, four roots are evaluated from the second equation, which are identified with the symbol $t_{f_1}^{\dot\omega_i}$. Again two of the four solutions are given by imposing $+\dot\omega_{max}$ while the other two by imposing $-\dot\omega_{max}$.

4.1.2. Maneuver Time for Step 2

The solution of t_{f_2} is carried out from the second set of equations in Equation (42). The two equations can be written as a function of the only variable t_{f_2}. In fact, the b_j coefficients of the polynomials, $t_{\omega_{max_2}}$ and $t_{\dot\omega_{max_2}}$ are functions of t_{f_2}. Therefore, the two equations can be written in an explicit form as a function of the time maneuver t_{f_2} by the following steps:

1. The b_j coefficients, stated in Equation (32), are replaced in Equation (29). As a consequence $\omega(t)$ and $\dot\omega(t)$ can be written as:

$$5\left(\frac{6\,\theta_f}{t_{f_2}^5}\right) t^4 - 4\left(\frac{15\,\theta_f}{t_{f_2}^4}\right) t^3 + 3\left(\frac{10\,\theta_f}{t_{f_2}^3}\right) t^2 = \omega_{max}$$

$$20\left(\frac{6\,\theta_f}{t_{f_2}^5}\right) t^3 - 12\left(\frac{15\,\theta_f}{t_{f_2}^4}\right) t^2 + 6\left(\frac{10\,\theta_f}{t_{f_2}^3}\right) t = \dot\omega_{max} \tag{46}$$

2. The conditions $t = t_{\omega_{max_2}} = t_{f_2}/2$ and $t = t_{\dot\omega_{max_2}} = (3 - \sqrt{3}) t_{f_2}/6$ are respectively substituted in the first and in the second expression of Equation (46). Thus, their final expressions as functions of t_{f_2} are obtained.

$$5\left(\frac{6\,\theta_f}{t_{f_2}^5}\right)\left(\frac{t_{f_2}}{2}\right)^4 - 4\left(\frac{15\,\theta_f}{t_{f_2}^4}\right)\left(\frac{t_{f_2}}{2}\right)^3 + 3\left(\frac{10\,\theta_f}{t_{f_2}^3}\right)\left(\frac{t_{f_2}}{2}\right)^2 = \omega_{max}$$

$$20\left(\frac{6\,\theta_f}{t_{f_2}^5}\right)\left(\frac{(3-\sqrt{3})t_{f_2}}{6}\right)^3 - 12\left(\frac{15\,\theta_f}{t_{f_2}^4}\right)\left(\frac{(3-\sqrt{3})t_{f_2}}{6}\right)^2$$

$$+ 6\left(\frac{10\,\theta_f}{t_{f_2}^3}\right)\left(\frac{(3-\sqrt{3})t_{f_2}}{6}\right) = \dot{\omega}_{max} \tag{47}$$

3. After several simplifications, Equation (47), can be written as follows

$$t_{f_2}^\omega = \frac{15}{8}\frac{\theta_f}{\omega_{max}}, \quad t_{f_2}^{\dot{\omega}} = \sqrt{\frac{10\sqrt{3}}{3}\frac{\theta_f}{\dot{\omega}_{max}}}. \tag{48}$$

The rest-to-rest guidance law gives two different solutions. $t_{f_2}^\omega$ and $t_{f_2}^{\dot{\omega}}$ are the final times which allow to verify $|\omega(t = t_{\omega_{max_2}})| = \omega_{max}$ and $|\dot{\omega}(t = t_{\dot{\omega}_{max_2}})| = \dot{\omega}_{max}$ respectively.

4.1.3. Maneuver Time for Step 3

The solution for t_{f_3} is evaluated from the third set of equations in Equation (42), by following the same strategy described in Section 4.1.1.

4.2. Final Strategy

Downstream of the analysis just performed, one can notice that it is necessary to select the optimal final time for each maneuver phase. The equations that have been described above result in many roots:

$$1 \to \begin{cases} |\omega_i(t = t_{\omega_{max_1}})| = \omega_{max} \to 6 \; roots \; (t_{f_1}^{\omega_i}) \\ |\dot{\omega}_i(t = t_{\dot{\omega}_{max_1}})| = \dot{\omega}_{max} \to 4 \; roots \; (t_{f_1}^{\dot{\omega}_i}) \end{cases}$$

$$2 \to \begin{cases} |\omega(t = t_{\omega_{max_2}})| = \omega_{max} \to 1 \; root \; (t_{f_2}^{\omega}) \\ |\dot{\omega}(t = t_{\dot{\omega}_{max_2}})| = \dot{\omega}_{max} \to 1 \; root \; (t_{f_2}^{\dot{\omega}}) \end{cases} \tag{49}$$

$$3 \to \begin{cases} |\omega_i(t = t_{\omega_{max_3}})| = \omega_{max} \to 6 \; roots \; (t_{f_3}^{\omega_i}) \\ |\dot{\omega}_i(t = t_{\dot{\omega}_{max_3}})| = \dot{\omega}_{max} \to 4 \; roots \; (t_{f_3}^{\dot{\omega}_i}) \end{cases}$$

Let us define n as roots of t_f^ω and m roots of $t_f^{\dot{\omega}}$, where the first solutions verify the condition $||\omega(t)|| \le \omega_{max}$, while the second ones the condition $||\dot{\omega}(t)|| \le \dot{\omega}_{max}$.

4.2.1. Selection of the Minimum Maneuver Times

Of all the n and m roots, only the real and positive ones are considered, while the complex and negative are discarded. Among the remaining, only the ones satisfying both constraints are maintained. The roots that verify both constraints could be selected by substituting the n roots in the constrain $||\dot{\omega}(t)|| \le \dot{\omega}_{max}$ and the m roots in the condition $||\omega(t)|| \le \omega_{max}$. Indeed, not all the roots verify both constraints, as a consequence some solutions can be discarded. This approach is schematized in the following:

$$(||\omega(t)|| \le \omega_{max}) \to n_{roots} \; of \; t_f^\omega \to (||\dot{\omega}(t)|| \le \dot{\omega}_{max}) \to l_{roots} \; of \; t_f^{\omega,\dot{\omega}}$$

$$(||\dot{\omega}(t)|| \le \dot{\omega}_{max}) \to m_{roots} \; of \; t_f^{\dot{\omega}} \to (||\omega(t)|| \le \omega_{max}) \to p_{roots} \; of \; t_f^{\omega,\dot{\omega}} \tag{50}$$

In general, only l of the n roots and p of the m roots verify both conditions, thus only the $(l+p)$ roots are suitable to obtain a feasible maneuver, satisfying the boundary conditions. The optimal solution is carried out by taking among the $l+p$ solutions the one corresponding

to the minimum time value. The method can be repeated for each kth step (with k = 1, 2, 3), and for each ith component (i = x, y, z) .

$$T_{f_k}^i = \min((l_{k,i} + p_{k,i})\, t_{f_k}^{\omega_i, \dot{\omega}_i}) \qquad (51)$$

where $T_{f_k}^i$ is the minimum final time of the kth step, for each ith component. The minimum time of each step is then evaluated by taking

$$T_{f_k} = \max_{i=x,y,z} \left(T_{f_k}^i \right) \qquad (52)$$

In this way, it is possible to find the kth solution that satisfies both the boundary conditions and the physical constraints Equations (4) and (9) in each step. T_{f_k} represents the duration time of each step and it was the problem's unknown. As a consequence, the coefficients of the three polynomials, which approximate the guidance law, are immediately evaluable by means of Equations (19) and (32) and the attitude guidance path of each step is solvable in a closed form, as reported in Equation (15) and in Equation (29).

4.2.2. Combining the Manoeuvres

In this section, the final maneuver strategy is presented. The total time of the guidance law presented could be shorter than the time at which the observation actually starts. This would seem to invalidate all the previous analyses. However, it is possible to implement a strategy to overcome the problem. Before showing it, some parameters must be introduced. The first is identified as Δt and represents the difference between the t_{start} and t_0, i.e.,

$$\Delta T = t_{start} - t_0, \qquad (53)$$

where t_{start} is the time when the target point acquisition should start and t_0 is the initial time of the $APPG$ maneuver. Hence, Δt represents the allowed maximum time to perform the maneuver. Since the strategy implemented has the purpose of obtaining a minimum time for each of the three steps, the total maneuver time ΔT_m can be defined as the sum of the times of each step (T_{f_k})

$$\Delta T_m = \sum_{k=1}^{3} T_{f_k} \qquad (54)$$

On one hand, maneuvers that do not fulfill the condition $\Delta T_m \leq \Delta T$ must be discarded because they require a longer maneuver time than the time in which the acquisition must begin. Therefore, these maneuvers are not feasible. On the other hand, if the condition $\Delta T_m \leq \Delta T$ is verified, it becomes useful to define another variable, named *waiting time*, representing the difference between the two total times:

$$t_w = \Delta T - \Delta T_m \qquad (55)$$

the *waiting time* represents a period in which the satellite could be in a stand-by mode before starting ground target acquisition. Thus, the *waiting time* must be included in the guidance law. The solution could be to perform it either at the beginning or at the end of the rest-to-rest phase (Figure 8), this does not compromise the guidance law proposed since in that conditions the angular velocities and accelerations are zero.

In the results section, the solution with the waiting phase at the end of the rest-to-rest maneuver has been chosen, but there would be no problem if the opposite solution were chosen. It is intended to emphasize the fact that this maneuver is certainly not possible without proper control to maintain the state of the satellite, which would otherwise tend to shift due to disturbances. However, this analysis is beyond the scope of this paper, since providing a control methodology is not part of the addressed problem. In fact, the proposed approach provides only the kinematic guidance of the satellite in terms of angular velocity and quaternion. Moreover, it is noteworthy that the choice of waiting without performing

any action during the *waiting time* is not the only one possible, as other activities could be done in the same time interval. For instance, the satellite could send data to the ground or place itself with the panels facing the sun, just by implementing a new *AGP*.
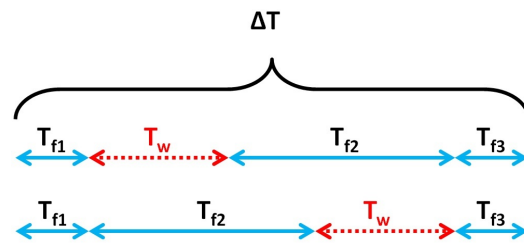

Figure 8. Maneuver strategy.

5. Simulation and Results

This section reports the results of the framework proposed in this work. All the tests have been performed using the MATLAB environment on an Intel Core I7-3610 CPU PC with a frequency of 2.30 GHz and 4 GB of RAM. In particular, a run of the *AGP* algorithm on this machine usually takes about 20 milliseconds. The specific guidance profile explored in the result section depends on the relative position between the satellite and the ground target (as reported in Figure 1). Specifically, the guidance profile depends on the motion of the satellite with respect to the ground target, i.e., it depends on the orbit parameters. The results section only reports one example with four ground targets to show the effectiveness of the proposed strategy. Different results would be obtained with different scenarios, but a more detailed discussion of the relationship between the results and different orbital regimes is beyond the scope of this paper. Moreover, it is worth pointing out that, as aforementioned, the attitude dynamics expression (in Equation (2)) is not simulated, since it is not used to evaluate the *AGP*, but only to derive the restrictions on the angular accelerations from restrictions on the control values (as shown in the Section 2.3). For this reason, the attitude dynamics is not introduced in the simulation environment, but only the orbital and Earth motion are considered as they are the only inputs needed for the *AGP* to evaluate the time-history of quaternions and angular velocities.

Simulations are performed to verify and validate the proposed analytical approach. To this aim, the SPICE Toolkit (provided by the California Institute of Technology) is used to generate the simulation environment in terms of orbital and Earth motion with respect to the ECI reference frame. The generation of the attitude guidance as well as the ground points tracked by the optical sensor are evaluated by using MatLab functions written by the authors. Hence, the quaternion guidance is also evaluated by implementing the proposed analytical approach.

5.1. Simulation Environment

The most important components of the SPICE system are the SPICE Toolkit software and the SPICE data files, often called "kernels". In this work the following kernels are used: `naif0012.tls`, `earth-200101-990628-predict.bpc`, `de438.bsp`, and `gm-de431.tpc`. In particular, these files contain the ephemeris of several satellites and the real displacement between *ECEF* and *ECI* reference frames as a function of seconds elapsed since midnight on November 17, 1858 (it is the date from which the counting of the modified Julian date begins). In particular, the simulation time was set from 26 Nov 2020 19:26:20 to 26 Nov 2020 19:56:20, and the SPOT-7 satellite has been chosen from SPICE files as a test case. SPOT-7, together with SPOT-6, forms a constellation of Earth-imaging satellites designed to provide continuity of high-resolution (the satellite physical parameters are reported in Table 2). Furthermore, the shape of the Earth is considered ellipsoidal with an equatorial radius equal to 6378.137 km and a polar radius equal to 6356.752 km by using the WGS84 model from SPICE. In this way, a high-precision geometry of the problem has been considered (it is reported in Figure 1).

Table 2. SPOT-7 parameters.

	Attitude Parameters	
I_x	Inertia along X_{BF}	603.896 (kg/m^2)
I_y	Inertia along Y_{BF}	565.396 (kg/m^2)
I_z	Inertia along Z_{BF}	318.792 (kg/m^2)
u_{max}	Maximum torque	0.5 (Nm)
$\dot{\omega}_{max}$	Maximum angular acceleration	0.0474 (deg/s^2)
ω_{max}	Maximum angular velocity	1 (deg/s)
	Orbit Parameters	
a	Semi-major axis	7075.945 (km)
e	Eccentricity	1.251×10^{-4}
e-04 i	Inclination	98.165 (deg)
$RAAN$	Right ascension of the ascending node	38.184 (deg)
AoP	Argument of periapsis	102.289 (deg)
ν	True anomaly	155.692 (deg)

The *ground targets* positions are identified by means of coordinates with respect to *ECEF* reference frame, expressed in terms of latitude (μ), longitude (λ), and altitude/elevation (h) above mean sea level. The *ground targets* are generated in a limited spatial area around the sub-satellite path. In particular, Figure 9 shows the location of the ground target points (on the south pole) and the thickness d, which identifies the allowed area within the ground points. The thickness d is set equal to 400 km, which corresponds to a rotation of 30 degrees with respect to the nadir. The number of target points N_t has been set equal to 4 (as shown in Figure 9). The latitude and longitude of the targets are then reported in Table 3.
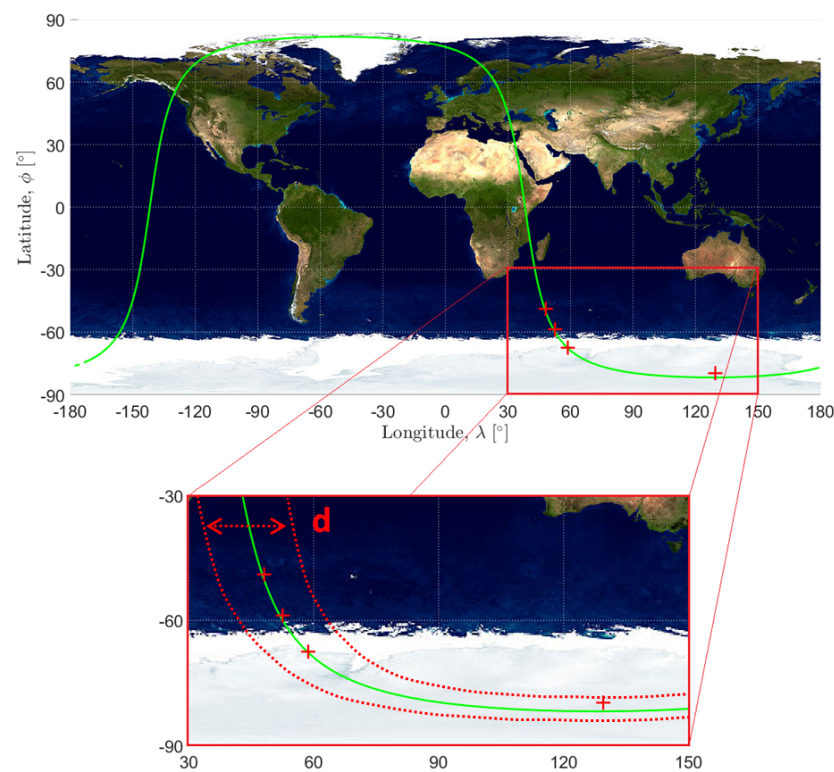

Figure 9. Sub-satellite trajectory (continuous green line) and ground targets (red cross) are reported on the top. The spatial band around the sub-satellite path (dashed red line) is shown in the enlarged graph below along with the thickness d.

Table 3. Ground target points.

	t_{start} (min)	LAT (deg)	LON (deg)	HEIGHT (m)
1	3.253	−79.783	129.459	91.452
2	9.557	−67.536	58.597	167.932
3	12.237	−58.779	52.500	942.248
4	15.320	−48.961	48.114	849.432

Finally, the *Payload* is an optical sensor in which the *PRF* is translated with respect to the *BF* reference frame by the vector $\overrightarrow{O_2O_3}$, while is rotated with a 3-2-1 set of Euler angles with respect to the *BF* reference frame by the mounted rotational matrix. The payload's parameters are summarized in Table 4, where t_{ac} is the exposure time required to acquire the ground target (i.e., it is the duration of the *ATPG* phase).

Table 4. Payload parameters.

Symbol	Description	Value
$\overrightarrow{O_2O_3}$	*PRF* displacement with respect to *BF*	[1 0.5 1] (m)
ϕ	*PRF* rotation with respect to X_{BF}	−30 (deg)
θ	*PRF* rotation with respect to Y_{BF}	−30 (deg)
ψ	*PRF* rotation with respect to Z_{BF}	0 (deg)
t_{ac}	Acquisition time	10 (s)

5.2. Simulation Results

In this section, the results are presented. In each figure, the APPG and the ATPG phases are indicated, respectively, with a continuous black and red line. Since the ATPG phase lasts much less than the other, in each figure a zoom of the results has been reported between point 3 and point 4 on the right side of the plot, so that the results are more intuitive and to underline the three APPG maneuvers mentioned in the previous section.

Figure 10 shows the attitude of the satellite with respect to *ECI*. The solution crosses all five desired points without any discontinuity, and the APPG phase is perfectly joined to the ATPG phase. This point can be better appreciated in the zoomed figure of the right part, where points 3 and 4 are shown more closely.

Figure 11 shows the path that is followed by the payload view axis (Z_{PRF} in green) in the *LVLH* reference frame, in order to acquire the target points 3 (blue) and 4 (red). The trajectory is descending, and one can notice that the Z_{PRF} axis starts pointing at the blue target (3) and then the red one (4) for the necessary time (in this case t_{ac} = 10 s, as reported in Table 4). Furthermore, referring to Table 3, it can be seen that the points are close to each other and the observations take place in a short time, against a run time of the algorithm of just 20 milliseconds. So it is possible to affirm that with this technique a new trajectory could be evaluated each time that a new target is required, thanks to the low computational time required. In the presented simulation, the physical constraints are completely satisfied. Figure 12 shows the components of the angular velocity, which never exceeds the admissible limit ω_{max} (indicated with a dot blue line), as well as it happens for the angular acceleration reported in Figure 13. Indeed, the angular acceleration reaches the maximum admissible value but never exceeds it. This solution agrees with the proposed analytical solution, which requires the maneuvers to be executed in near-minimum time by solving Equation (42). Moreover, the imposed kinematic constraints also guarantee that the ideal required control torque for the maneuvers implementation is confined within the maximum limits admissible. This result can be seen in Figure 14, where the ideal control policy (given as summation of $\mathbf{u}_c$ and $\mathbf{u}_p$ and indicated as $\mathbf{U} = [U_x, U_y, U_z]$) from

Equation (2) for the APPG and ATPG phases are respectively represented by a continuous black and red line, while the maximum boundaries are indicated with two dot blue lines. As happened for the angular velocity and acceleration, the control also almost reaches the maximum admissible value.
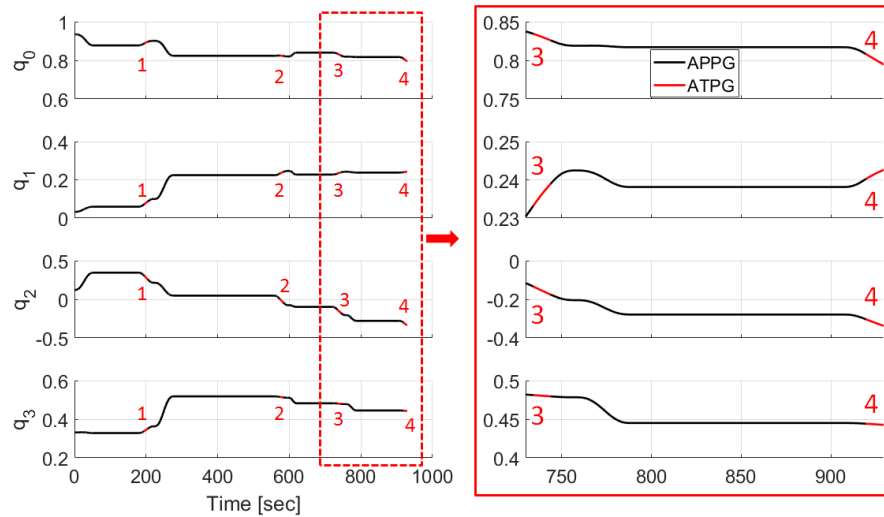

Figure 10. Attitude generated by APPG (black) and ATPG (red) to acquire four ground targets.
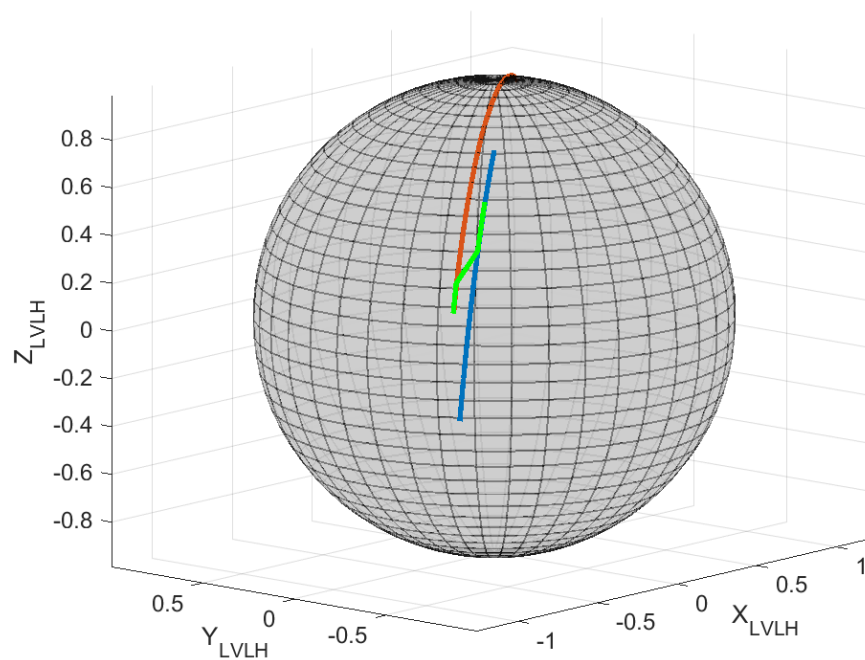

Figure 11. Representation of Z_{PRF} (green) and the $\widehat{O_3 T}$ of the point 3 (blue) and 4 (red) with respect to the *LVLH* reference frame.
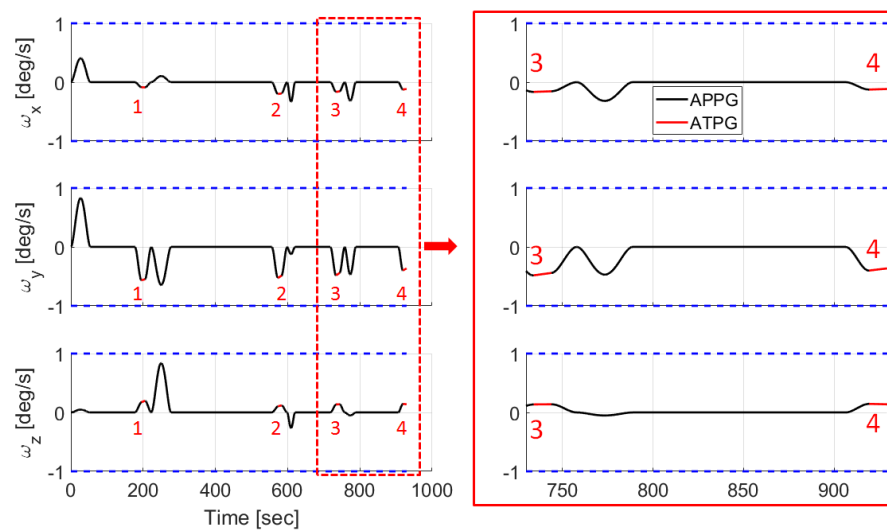
Figure 12. Angular velocity generated by APPG (black) and ATPG (red) to acquire four ground targets.
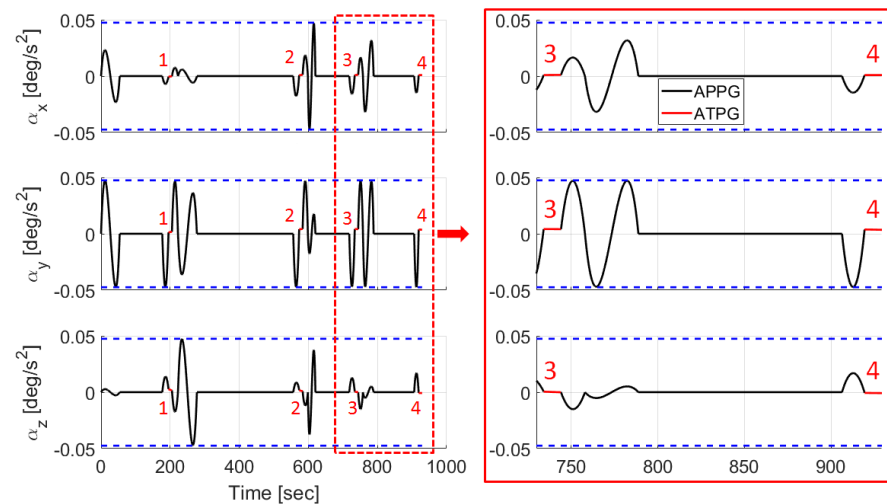

Figure 13. Angular acceleration generated by APPG (black) and ATPG (red) to acquire four ground targets.
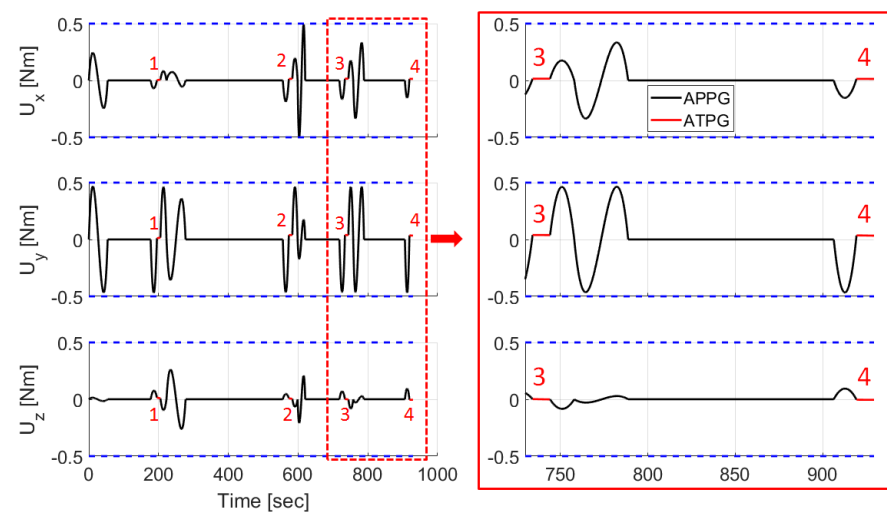

Figure 14. Control torque generated by APPG (black) and ATPG (red) to acquire four ground targets.

6. Conclusions

In this work, an analytical solution for multiple ground target point acquisitions has been presented. In general, the attitude generator planned (AGP) must generate the guidance that first brings the satellite to the right position and then leads it in the right pointing path. Hence, the proposed technique consists of two different parts: the attitude target pointing generator ($ATPG$) and the attitude point-to-point generator ($APPG$). The first one finds a geometrical solution to generate the pointing trajectory in order to acquire the ground targets, while the second phase generates the target-tracking trajectory during the acquisition time interval. An analytical solution is found by approximating the angular velocity and acceleration with polynomials. This strategy gives the possibility to satisfy both boundary conditions and physical constraints. The results reported in this work demonstrate the effectiveness of the proposed approach, as the provided solution can rapidly point the satellite to successive targets and track them for the time needed for the acquisition. It is worth noting that all the constraints and boundary conditions are satisfied as they are directly imposed into the solving equation. Finally, the algorithm is suitable for possible future implementation in real on-board flight hardware given the fact that a closed-form solution with simple analytical calculations has been attained.

Author Contributions: Conceptualization: A.C.; methodology: A.C., D.S. and F.C.; software: A.C.; validation: A.C.; formal analysis: A.C.; investigation: A.C.; resources: A.C. and F.C.; writing—original draft preparation: A.C.; writing—review and editing: A.C. and F.C.; visualization: A.C.; supervision: A.C. and F.C. All authors have read and agreed to the published version of the manuscript.

Institutional Review Board Statement: Not applicable.

Informed Consent Statement: Not applicable.

Data Availability Statement: Not applicable.

Conflicts of Interest: The authors declare no conflict of interest.

References

1. Campbell, J.B. Introduction to remote sensing. In *Introduction to Remote Sensing*; Guilford Press: New York, NY, USA, 1987.
2. Press, N.A. *Earth Observations from Space: The First 50 Years of Scientific Achievements*; National Academies Press: Washington, DC, USA, 2008; pp. 1–130. [CrossRef]
3. Chuvieco, E. *Earth Observation of Global Change: The Role of Satellite Remote Sensing in Monitoring the Global Environment*; Springer: Berlin, Germany, 2008; pp. 1–223. [CrossRef]
4. Li, Z.; Tomás, R. Earth Observations for Geohazards; MDPI: Basel, Switzerland, 2017. [CrossRef]
5. D'Errico, M. *Distributed Space Missions for Earth System Monitoring*; Springer: New York, NY, USA, 2013; pp. 1–675. [CrossRef]
6. Kornfeld, R. On-board autonomous attitude maneuver planning for planetary spacecraft using genetic algorithms. In Proceedings of the AIAA Guidance, Navigation, and Control Conference and Exhibit, Austin, TX, USA, 11–14 August 2003; p. 5784.
7. Wu, C.; Xu, R.; Zhu, S.; Cui, P. Time-optimal spacecraft attitude maneuver path planning under boundary and pointing constraints. *Acta Astronaut.* **2017**, *137*, 128–137. [CrossRef]
8. Wu, C.; Han, X. Energy-optimal spacecraft attitude maneuver path-planning under complex constraints. *Acta Astronaut.* **2019**, *157*, 415–424. [CrossRef]
9. Melton, R.G. Hybrid methods for determining time-optimal, constrained spacecraft reorientation maneuvers. *Acta Astronaut.* **2014**, *94*, 294–301. [CrossRef]
10. Spiller, D.; Melton, R.G.; Curti, F. Inverse dynamics particle swarm optimization applied to constrained minimum-time maneuvers using reaction wheels. *Aerosp. Sci. Technol.* **2018**, *75*, 1–12. [CrossRef]
11. Spiller, D.; Ansalone, L.; Curti, F. Particle swarm optimization for time-optimal spacecraft reorientation with keep-out cones. *J. Guid. Control. Dyn.* **2016**, *39*, 312–325. [CrossRef]
12. Zhang, G.; Li, X.; Hu, G.; Zhang, Z.; An, J.; Man, W. Mission Planning Issues of Imaging Satellites: Summary, Discussion, and Prospects. *Int. J. Aerosp. Eng.* **2021**, *2021*, 7819105. [CrossRef]
13. Florio, S.; Zehetbauer, T.; Neff, T. Optimal operations planning for SAR satellite constellations. In Proceedings of the Low Earth Orbit. 6th International Symposium on Reducing the Costs of Spacecraft Ground Systems and Operations, ESOC, Darmstadt, Germany, 14–17 June 2005..
14. Stock, G.; Fraire, J.; Hermanns, H.; Cruz, E.; Isaacs, A.; Imbrosh, Z. On the Automation, Optimization, and In-Orbit Validation of Intelligent Satellite Constellation Operations. *IEEE Trans. Comput.-Aided Des. Integr. Circuits Syst.* **2021**, *39*, 3762–3773. [CrossRef]

15. Song, Y.; Huang, D.; Zhou, Z.; Chen, Y. An emergency task autonomous planning method of agile imaging satellite. *EURASIP J. Image Video Process.* **2018**, *2018*, 1–11. [CrossRef]

16. Liu, S.; Yang, J. A satellite task planning algorithm based on a symmetric recurrent neural network. *Symmetry* **2019**, *11*, 1373. [CrossRef]

17. Lai, L.C.; Yang, C.C.; Wu, C.J. Time-optimal maneuvering control of a rigid spacecraft. *Acta Astronaut.* **2007**, *60*, 791–800. [CrossRef]

18. Weiguo, Z.; Pingyuan, C.; Hutao, C. Autonomous Attitude Maneuver Planning for Spacecraft under Complex Constraints (TN). *Acta Aeronaut. Astronaut. Sin.-Ser. A B* **2007**, *28*, 1091.

19. Wie, B.; Bailey, D.; Heiberg, C. Rapid multitarget acquisition and pointing control of agile spacecraft. *J. Guid. Control. Dyn.* **2002**, *25*, 96–104. [CrossRef]

20. Zhou, H.; Wang, D.; Wu, B.; Poh, E.K. Time-optimal reorientation for rigid satellite with reaction wheels. *Int. J. Control.* **2012**, *85*, 1452–1463. [CrossRef]

21. Xu, R.; Wu, C.; Zhu, S.; Fang, B.; Wang, W.; Xu, L.; He, W. A rapid maneuver path planning method with complex sensor pointing constraints in the attitude space. *Inf. Syst. Front.* **2017**, *19*, 945–953. [CrossRef]

22. Calaon, R.; Schaub, H. Constrained Attitude Maneuvering via Modified-Rodrigues-Parameter-Based Motion Planning Algorithms. *J. Spacecr. Rocket.* **2022**, *59*, 1–15. [CrossRef]

23. Dearing, T.L.; Hauser, J.; Chen, X.; Nicotra, M.M.; Petersen, C. Efficient Trajectory Optimization for Constrained Spacecraft Attitude Maneuvers. *J. Guid. Control. Dyn.* **2022**, *45*, 638–650. [CrossRef]

24. Li, Z.; Zhao, L.; Liu, Y.; Chen, X.; Chen, H.; Zheng, F.; Zhang, Y.; Wang, D.; Li, J.; Liu, J.; et al. Autonomous Mission Planning Method for Optical Imaging Satellites Based on Real-Time Cloud Cover Information. *Remote Sens.* **2022**, *14*, 2635. [CrossRef]

25. He, Y.; Wang, Y.; Chen, Y.; Xing, L. Auto mission planning system design for imaging satellites and its applications in environmental field. *Pol. Marit. Res.* **2016**, *23*, 59–70. [CrossRef]

26. Sandau, R.; Röser, H.P.; Valenzuela, A. *Small Satellites for Earth Observation*; Springer: Berlin, Germany, 2008; pp. 1–406. [CrossRef]

27. Rosso, M.P.D.; Ullo, S.L.; Sebastianelli, A.; Spiller, D.; Puglisi, E.; Martire, D.D.; Aparício, S.; Addabbo, P. Artificial intelligence, machine learning and deep learning. In *Artificial Intelligence Applied to Satellite-Based Remote Sensing Data for Earth Observation*; IET Digital Library: London, UK, 2021; pp. 39–61. [CrossRef]

28. Rosso, M.P.D.; Ullo, S.L.; Sebastianelli, A.; Spiller, D.; Puglisi, E.; Biondi, F.; Orlando, D. Artificial neural network. In *Artificial Intelligence Applied to Satellite-Based Remote Sensing Data for Earth Observation*; IET Digital Library: London, UK, 2021; pp. 63–90. [CrossRef]

29. Ullo, S.L.; Sebastianelli, A.; Rosso, M.P.D.; Spiller, D.; Puglisi, E.; Nowakowski, A.; Bernardi, M.L.; Cimitile, M. Convolutional neural networks. In *Artificial Intelligence Applied to Satellite-Based Remote Sensing Data for Earth Observation*; IET Digital Library: London, UK, 2021; pp. 91–111. [CrossRef]

30. Sebastianelli, A.; Rosso, M.P.D.; Zarro, C.; Martire, D.D.; Napoli, M.D.; Spiller, D.; Nowakowski, A.; Bonifacio, R.; Kim, D.H.; Garcia-Herranz, M. A classification problem. In *Artificial Intelligence Applied to Satellite-Based Remote Sensing Data for Earth Observation*; IET Digital Library: London, UK, 2021; pp. 159–206. [CrossRef]

31. Rosso, M.P.D.; Sebastianelli, A.; Spiller, D.; Mathieu, P.P.; Ullo, S.L. On-Board Volcanic Eruption Detection through CNNs and Satellite Multispectral Imagery. *Remote Sens.* **2021**, *13*, 3479. [CrossRef]

32. Giuffrida, G.; Fanucci, L.; Meoni, G.; Batic, M.; Buckley, L.; Dunne, A.; Dijk, C.V.; Esposito, M.; Hefele, J.; Vercruyssen, N.; et al. The Φ-Sat-1 Mission: The First On-Board Deep Neural Network Demonstrator for Satellite Earth Observation. *IEEE Trans. Geosci. Remote Sens.* **2022**, *60*, 5517414. [CrossRef]

33. Spiller, D.; Ansalone, L.; Carotenuto, F.; Mathieu, P.P. Crop Type Mapping Using Prisma Hyperspectral Images and One-Dimensional Convolutional Neural Network. In Proceedings of the 2021 IEEE International Geoscience and Remote Sensing Symposium IGARSS, Brussels, Belgium, 11–16 July 2021. [CrossRef]

34. Spiller, D.; Ansalone, L.; Amici, S.; Piscini, A.; Mathieu, P.P. Analysis and detection of wildfires by using prisma hyperspectral imagery. *Int. Arch. Photogramm. Remote. Sens. Spat. Inf. Sci.* **2021**, *43*, 215–222. [CrossRef]

35. Spiller, D.; Ansalone, L.; Longépé, N.; Wheeler, J.; Mathieu, P.P. Wildfire detection and monitoring by using PRISMA hyperspectral data and convolutional neural networks. In Proceedings of the EGU General Assembly 2021, Online, 19–30 April 2021; EGU21-12330. [CrossRef]

36. Wertz, J.R. *Spacecraft Attitude Determination and Control*; Springer Science & Business Media: Berlin, Germany, 2012; Volume 73.

37. Yang, Y. *Spacecraft Modeling, Attitude Determination, and Control: Quaternion-Based Approach*; CRC Press: Boca Raton, FL, USA, 2019. [CrossRef]

38. Vallado, D.A. *Fundamentals of Astrodynamics and Applications*; Springer Science & Business Media: Berlin, Germany, 2001; Volume 12.

39. Markley, F.L.; Crassidis, J.L. *Fundamentals of Spacecraft Attitude Determination and Control*; Springer: Berlin/Heidelberg, Germany, 2014; Volume 33.

40. Neumark, S. *Solution of Cubic and Quartic Equations*; Elsevier: Amsterdam, The Netherlands, 2014.